



www.DeepakPublishing.com

Baird, M. J. and Lemmer, K. M. (2018): JoSS, Vol. 7, No. 1, pp. 665–681  
(Peer-reviewed article available at [www.jossonline.com](http://www.jossonline.com))



www.JoSSonline.com

# Investigation of the Effect of Gimbaling and Magnetic Attitude Control on an Integrated CubeSat Ion Thruster

Matthew J. Baird and Kristina M. Lemmer

*Western Michigan University Aerospace Laboratory for Plasma Experiments  
Kalamazoo, Michigan*

---

## Abstract

Ion thrusters are a viable candidate for CubeSat integration and can provide high specific impulse/low thrust for station-keeping, attitude control, and orbital maneuvers. In addition to incorporating a thruster into the CubeSat design, it may be necessary to use passive or active magnetic attitude control simultaneously with the propulsion system. An investigation of the potential for integrating micro RF ion thrusters on a CubeSat platform was conducted at Western Michigan University's Aerospace Laboratory for Plasma Experiments to understand the interactions between an electric propulsion system, magnetic attitude control systems (ACS), and the CubeSat chassis. A  $\theta$ -R plasma probe positioning system combined with a magnetorquer positioning and thruster gimbaling system were controlled, while probe data and continuous telemetry data were recorded. The thruster operated between 5.8 and 7.74 W, and the mean ion energy level was 1783 eV. The CubeSat chassis floating potential remained between 7.9 and 9.3 V, increasing as the magnetic ACS moved toward the thruster. Changes in screen and acceleration grid currents during ACS positioning and gimbaling were constant to within measurement errors. Thruster gimbaling resulted in little change of the thruster plume profile; however, a depression in current density and floating and plasma potentials was visible at  $-30^\circ$  off thruster centerline, which corresponds to the placement of an asymmetric cathode.

---

## 1. Introduction

CubeSats have grown in popularity from university training tools to platforms for robust science and technology demonstration missions. There is increasing interest from industry, the military, and NASA to use the CubeSat platform. The increased demand for CubeSat capabilities has resulted in the requirement that CubeSats have onboard propulsion systems for orbit maneuvers, attitude control, reaction wheel desaturation, proximity operations, and station-keeping.

However, there are still several constraints that limit the capabilities of CubeSat propulsion systems, namely size and launch restrictions that require range safety waivers that can be difficult to obtain. Range safety restrictions include ignition sources, amount of stored chemical energy, and limits to pressure vessels. Several thruster technologies have been developed (Lemmer, 2017; Sarda et al., 2006; Zandbergen and Cervone, 2014; Bani, 2016; Grönland et al., 2014; Rangsten, Bejhed, and Johansson, 2012;

Corresponding Author: [kristina.lemmer@wmich.edu](mailto:kristina.lemmer@wmich.edu)

Kronhaus et al., 2013), and a limited number of those have been tested in orbit to provide CubeSats with only minor capabilities, such as the ability to de-tumble (Pukniel et al., 2011; Steyn and Lappas, 2011; Rankin et al., 2005; Hinkley, 2017; Guo, Bouwmeester, and Gill, 2016).

Thruster development for CubeSats has been heavily focused on electric propulsion (EP). EP thruster technology is varied in its application, and EP thrusters have the ability to operate on solid, liquid, and gaseous inert propellants. Implementing EP devices onto CubeSats presents unique challenges due to the small volume of a CubeSat. Mission critical payload components must function in close proximity to the propulsion system. Furthermore, magnetic circuits and electronic components onboard the spacecraft may be affected, or may affect applied and induced magnetic fields necessary for successful operation of the EP system. Potential interactions between onboard subsystems, EP systems, and the plasma plume must be characterized to ensure limited long-term system degradation of the satellite.

One EP technology that is relatively simple to miniaturize is the gridded ion thruster. Several small DC and RF gridded ion thrusters have been developed (Gollor and Boss, 2006; Leigh et al., 2013; Chen, 2014; Wirz et al., 2008). The work presented here focuses on a 1-cm-diameter RF gridded ion thruster (Tsay et al., 2012). The thruster is nominally rated for 185  $\mu\text{N}$  of thrust with a specific impulse of 1600 s, operating at about 10 W of RF power at approximately 8.5 MHz using 0.06 sccm of xenon. A thermionic emitting cathode designed to output 50 mA was used to neutralize the plasma plume and provide seed electrons for starting the thruster. The cathode was integrated onto the CubeSat structure inside of a vacuum chamber (HeatWaveLabsInc, 2002; Goebel and Katz, 2008). The structure was outfitted with an active magnetic attitude control system (ACS). For the active ACS, magnetorquers use the combined magnetic field of three orthogonal electromagnets (Candinia et al., 2012). Passive magnetic stabilization can also be used for ACS, where permanent magnets are used in place of electromagnets (Gerhardt et al., 2017). Previous simulation work, shown in Figure 1, implies that the applied ACS

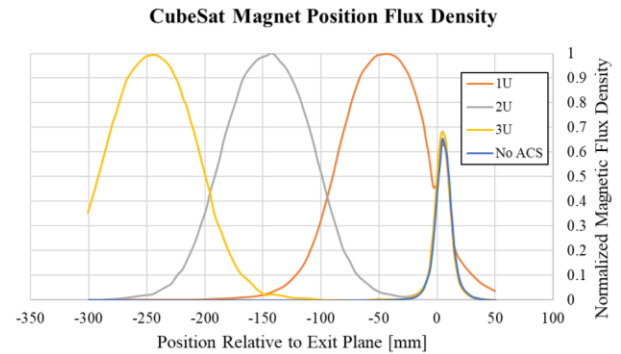


Figure 1. Combined magnetic field behavior of a magnetic ACS and RF ion thruster (Hine, 2016).

magnetic fields will interact with the magnetic field induced by the RF coil in the ion thruster at satellite sizes smaller than 2U (Hine, 2016). This work will determine whether that interaction affects thruster operation. Thrust vectoring was also investigated to determine the extent to which the thruster can be vectored before the plasma plume begins affecting the spacecraft body. Thruster telemetry data were recorded for a variety of operating conditions of the magnetorquers, including values that represent magnetic fields common for passive ACS (Rawashdeh, 2010; Springmann et al., 2012; Ovchinnikov et al., 2000) and active ACS (Scholz et al., 2017; Ovchinnikov et al., 2007). The plasma plume was studied with a Faraday probe, a Langmuir Probe (LP), and an energy analyzer.

## 2. Experimental Setup

The experiment was conducted at Western Michigan University's Aerospace Laboratory for Plasma Experiments (ALPE) in a 1.5-meter-long, 1-meter-diameter cylindrical vacuum chamber. The chamber was outfitted with a single CTI-250 cryogenic pumping system with a base pressure of  $1\text{E-}7$  Torr.

### 2.1. Electrical Configuration and Positioning Systems

The CubeSat chassis and ACS were mounted to a separate rotary and linear table system from that used for the plasma diagnostic probes. Using a ceramic electrical break, the CubeSat chassis was electrically

floating, and its potential was monitored using a 6.5 digit digital multimeter. The CubeSat was mechanically coupled to the gimbal rotary table; however, the ACS was coupled to both the gimbal rotary table and the ACS positioning table. This resulted in the ability to rotate both the CubeSat chassis and attitude control system as one unit, while still being able to adjust the distance between the ACS and the thruster. This two-table system was the mechanism by which the thrust vector angle was adjusted and different CubeSat sizes were simulated during the experiment. The RF ion thruster was mounted to the chamber through a polymer electric break. The thruster body is MACOR ceramic, and no thruster electrical common exists. See Figure 2 for details of the experimental electrical configuration.

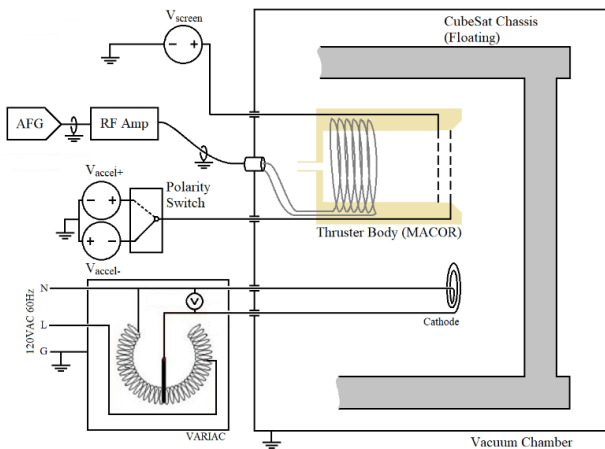


Figure 2. Electrical diagram of the thruster and cathode. The ceramic thruster body and CubeSat chassis are electrically floating.

Through all experiments, the thruster remained stationary and did not rotate. Rather than articulating the thruster, the combined motion of the CubeSat chassis and ACS emulated thrust vectoring in an effort to eliminate the effects of the thruster angle with respect to the vacuum chamber walls. The thrust vector angle was set to  $0^\circ$ ,  $2^\circ$ ,  $5^\circ$ , and  $10^\circ$  from the primary thrust vector. The gimbal rotary table, the probe rotary table, and the CubeSat chassis all lay collinear on the y (vertical)-axis with the thruster face positioned 50 mm forward of this line. The plasma probes, thruster, CubeSat chassis, and ACS lay collinear along the z (axial)-axis. See Figures 3 and 4 for

a simplified diagram and photograph of the experimental setup, respectively.

## 2.2. RF Ion Thruster and Cathode

The RF ion thruster was nominally operated between 8.3 and 8.5 MHz. The frequency was set on a function generator, and the signal was passed through an RF amplifier. Due to characteristic impedance changes from the coupled plasma and rise in temperature, additional adjustment of RF frequency was performed to minimize the RF power standing wave ratio (SWR) after the thruster was started and before experimental data were obtained. This additional adjustment was typically under 0.07 MHz. The screen and acceleration grids were set to 1800 V and  $-200$  V, respectively. During thruster operation, forward and reverse power, acceleration grid voltage and current, screen grid voltage and current, and facility pressure were continuously recorded. The RF ion thruster was located along the centerline of the CubeSat chassis, as shown in Figure 5.

The 1-cm RF ion thruster required seed electrons to begin thruster operation and required plasma plume neutralization. These were provided by a thermionic cathode with an emitter liquid cathode coating located below and to the side of the thruster, as shown in Figure 5. The cathode coating contained diluted barium and strontium carbonates suspended in a Xylol-Butanol. It was applied to a 152 mm length of 0.508 mm-diameter tungsten wire, shaped into a planer coil. A conversion process consisting of volatile product evaporation, carbonate to oxide conversion, and final stabilization occurred through a careful heating process. The thermionic cathode was powered with 16 watts of AC power, and the temperature of the cathode was estimated by assuming a simple black body radiation model. Figure 5b shows a photograph of the cathode in its installed location in the vacuum chamber next to the thruster.

## 2.3. Magnetorquers

An active three-axis magnetorquer was created to simulate the effect of active magnetic stabilization on the thruster operational telemetry. The X- and Y-axis

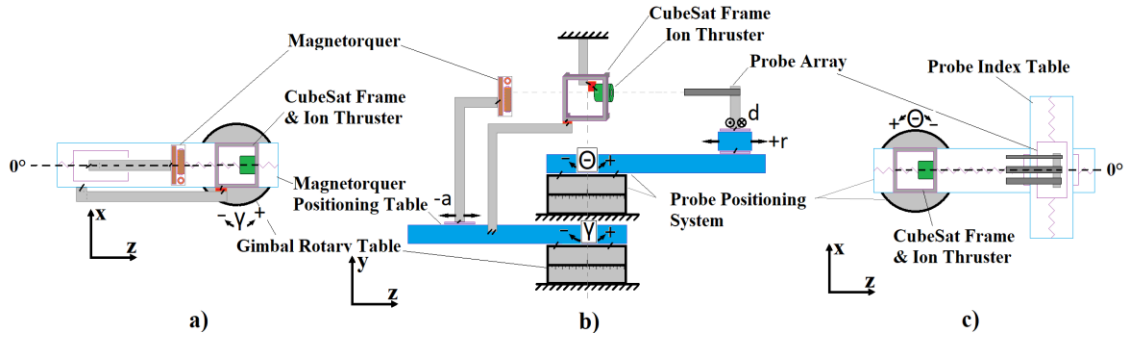


Figure 3. Experimental setup inside the ALPE vacuum chamber. Three linear tables and two rotary tables allow for wide  $\theta$ -R probe sweeping, magnetorquer positioning, and thruster gimbaling. a) Top view of the magnetorquer positioning and gimbaling tables only. The gimbaling datum angle is marked. b) A profile view of the complete probe, gimbal and magnetorquer positing system, c) Top view of the probe positioning system only. The probe array datum used in probe maps is marked.

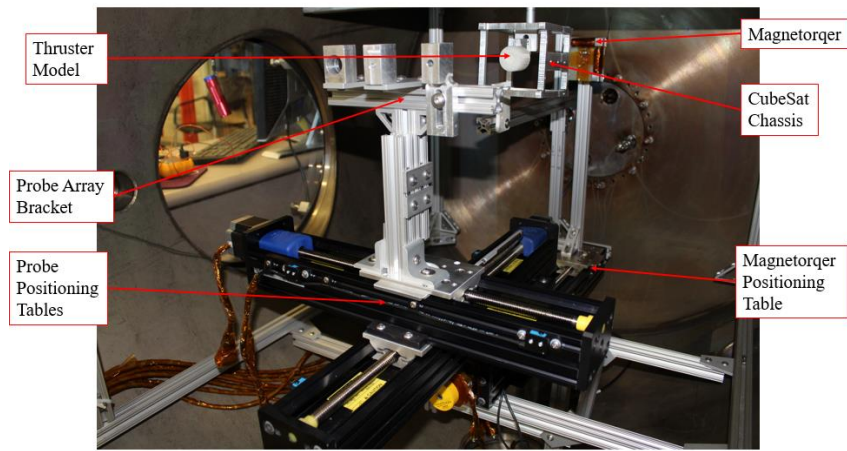


Figure 4. Photograph of the experimental setup without electrical or gas hookups. The photograph contains a 3D printed thruster model that was created to minimize risk of thruster damage during installation.

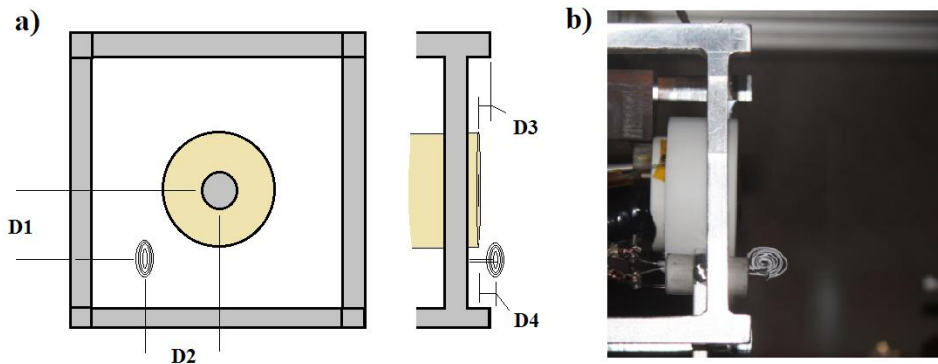


Figure 5. Front and Profile view and dimensions of the thruster and cathode within the experimental setup. D1=30.0 mm, D2=23.6 mm, D3=2.0 mm, D4=6mm.

magnet coils contain 200 turns of 22 AWG magnet wire 44.45 mm in length, wound around a 6.35-mm-diameter ferrite core. They were mounted to the front

of an FR4/G10 fiberglass support structure. The Z-axis magnet is 1 cm long with a vacuum core of cross sectional area 64 mm by 64 mm, and used 30 turns of

the same magnet wire. It was attached to the back of the FR4 support. Figure 6a shows the location of the magnetorquer with respect to the RF ion thruster. The assembly was mounted on a translation table, so that it could be positioned based on a variety of CubeSat sizes, ranging from 1.5U to 3U. The distance measured from the back of the CubeSat chassis to the FR4 component of the magnetorquer ranged from 56 mm to 190 mm. Figure 6b shows the relative positions of the magnetorquer with respect to the CubeSat structure and thruster.

The estimated magnetic moment produced by the X and Y coils with the application of 1.5 A is  $0.085 \text{ Am}^2$ . The estimated Z coil magnetic moment for the same current is  $0.4 \text{ Am}^2$ . This is comparable to existing magnetorquer designs and commercial off the shelf products (Jayaram, 2010).

## 2.4. Diagnostics Probes

A diagnostic plasma probe array containing an LP, a Faraday probe, and a retarding potential analyzer (RPA) was used to study the thruster plume. The probes were positioned using two linear tables and a rotary table to create a typical  $\theta$ -R probe array positioning system. The experimental setup swept the probes between  $-90^\circ$  and  $+60^\circ$  from the primary thrust vector, and positioned the probes from 37 mm to 267 mm downstream of the thruster face, as shown in Figure 3. The probe array is shown in Figure 7a, downstream of the thruster.

The LP (Figure 7b) is a 6.35-mm-long by 0.25-

mm-diameter tungsten electrode that is swept from -15 V to 200 V while immersed in the plasma plume. Current is collected as a function of voltage, and these current vs. voltage sweeps allow for the calculation of ion number density, electron temperature, plasma potential, and floating potential of the thruster plume. The Faraday probe is a  $-20 \text{ V}$  biased electrode surrounded by a  $-20 \text{ V}$  biased shield, as shown in Figure 7c. The electrode is a tungsten-coated, 6.33-mm-diameter collecting disc surrounded by a tungsten coated annulus guard with an outer diameter of 13 mm. There is a 0.83 mm gap between the inner collector and outer guard. As the probe is swept through the thruster plume, current is recorded. Faraday probe data yield accurate qualitative plasma plume mapping, which shows the divergence characteristics of the exhaust plume. Last, the RPA (Figure 7d) yields an indication of the energy of ions leaving the thruster. The RPA uses an orifice diameter of 6.35 mm, and consists of four grids and a collector plate. The grids, shown in Figure 7d are: A) a floating grid to ensure that the probe has minimum impact on the plasma; B) an electron repelling grid, biased to  $-60 \text{ V}$  to prevent electrons from entering the probe; C) an ion retarding grid, swept from 0 V to 2100 V to filter ions by energy; and D) an electron suppression grid, biased to  $-60 \text{ V}$  to minimize secondary electron emission from the collector plate.

The diagnostic probes were aligned such that the FP and RPA were coplanar with the LP electrode midpoint. The distance between the FP and RPA centerlines was 47.5 mm, and the distance between

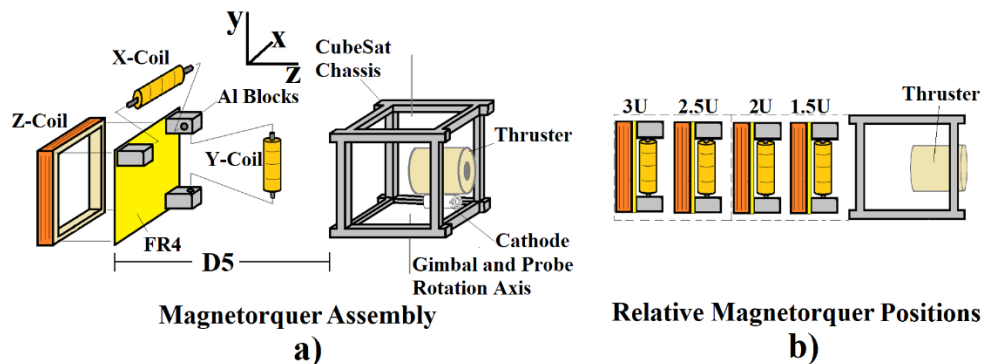


Figure 6. a) Magnetorquer assembly and axis orientation of the experiment. The dimension D5 ranged from 56.3 mm to 190 mm to position the magnetorquer at CubeSat sizes ranging from the 1.5U to 3U. b) Relative position of the magnetorquer to the CubeSat chassis.

the RPA and LP centerlines was 50.7 mm, as shown in Figure 7e.

### 2.5. Thruster Operating Parameters

Telemetry data were continuously monitored and logged at a frequency of 7 Hz, and a period of five minutes elapsed after thruster startup before experiments were performed. An average of 500 steady state telemetry measurements were documented at each gimbal angle. An average of 900 steady state telemetry measurements were documented at each magnetorquer position. For each gimbaling telemetry data set, acceleration and screen grid currents had a standard deviation of less than 0.01 mA. RF power deviated less than 0.23W over the same data sets.

Table 1 shows the nominal thruster operating conditions while sweeping the LP, Faraday probe, and RPA. During FP and LP probe sweeping, telem-

etry measurements for forward and reverse power deviated 4% and 8% from the mean value, respectively. During RPA testing, forward and reverse power deviated 18% and 3% percent, respectively. During probe data collection, acceleration and screen grid currents had a standard deviation of less than 0.053 mA during probe measurements.

### 3. Data Analysis

All data were collected using a LabView script and saved in a spreadsheet format for later analysis. Data analysis was performed in several MatLab scripts created for each type of probe data.

Faraday probe data were collected as ten individual current readings at each location that were averaged. A dimensional correction factor was applied to compensate for line-of-sight effective probe area changes that were caused by the difference between

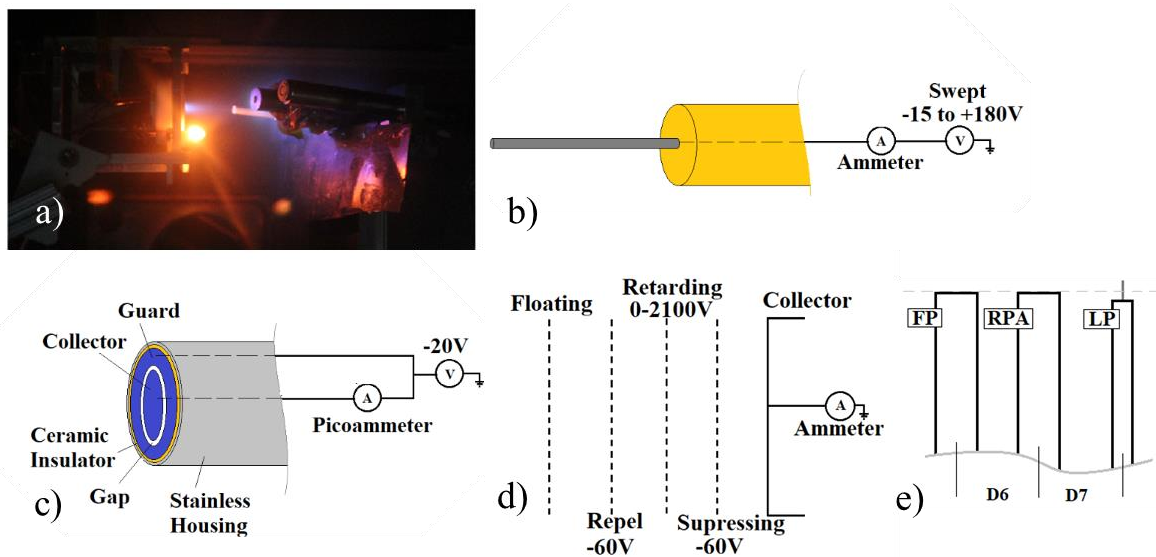


Figure 7. a) Photograph of probe array in position downstream of the thruster. b) LP diagram. c) Faraday probe diagram. d) Cross section of the retarding potential analyzer probe with voltages applied to each grid. e) Relative probe position. D6 is 47.5 mm and D7 is 50.7 mm. Both Faraday and RPA probes were coplanar with the mid length point of the LP.

Table 1. Average Thruster Operating Parameters During Probe Plume Mapping Experiments

| Probe | Cathode Power, W | Thruster mass flow rate, sccm | Screen potential, V | Screen current, mA | Accel potential, V | Accel current, mA | RF             |                  |                  | Pressure, Torr |
|-------|------------------|-------------------------------|---------------------|--------------------|--------------------|-------------------|----------------|------------------|------------------|----------------|
|       |                  |                               |                     |                    |                    |                   | Frequency, MHz | Forward Power, W | Reverse Power, W |                |
| LP    | 9.00             | 0.30                          | 1857                | 1.79               | -218               | -0.14             | 8.37           | 7.36             | 1.60             | <6.1E-6        |
| FP    | 9.00             | 0.30                          | 1799                | 1.36               | -220               | -0.15             | 8.34           | 7.74             | 1.60             | 4.1E-06        |
| RPA   | 9.00             | 0.30                          | 1802                | 1.14               | -199               | -0.18             | 8.30           | 5.80             | 1.45             | <6.1E-6        |

the probe sweeping rotation point and thruster exit plane location. Ion beam current,  $I_{Beam}$ , was calculated by integrating the Faraday probe collected current,  $I_{probe}(\theta)$  over a  $90^\circ$  sweep at a probe radius,  $R$ , of 37 mm, using Equation (1) (Brown et al., 2016):

$$I_{Beam} = 2\pi R^2 \int_{\theta=-90}^{\theta=0} \frac{I_{probe}(\theta)}{A_{eff}} \sin \theta \, d\theta, \quad (1)$$

where  $A_{eff}$  is the effective probe area due to the changes in relative angle between the thruster face and the probe face over the sweep range, and  $\theta$  is the sweep angle that ranged from  $-90$  to  $0$  degrees. This ion beam current is used to estimate thrust,  $T$ , using Equation (2):

$$T = \sqrt{\frac{2M_i}{e}} I_{Beam} \sqrt{V_{Beam}}, \quad (2)$$

where  $M_i$  is ion mass,  $e$  is the charge of an electron, and  $V_{Beam}$  is the net beam voltage, which is given as the difference between the screen and plasma potentials. For xenon gas  $\sqrt{2M_i/e} = 1.65$  (Goebel and Katz, 2008). Beam potential was found from LP data as the average at an arc located 37 mm in front of the thruster and spanning all effective LP traces.

LP current versus voltage (I-V) traces were processed according to Lobbia and Beal (2016). The Debye length,  $\lambda_D$ , is used to determine the operating regime of the LP. The LP can operate in thin sheath, where  $\frac{r_p}{\lambda_D} > 50$ ; transitional sheath,  $3 < \frac{r_p}{\lambda_D} < 50$ ; orbital motion limited (OML),  $r_p/\lambda_D < 3$ . The LP in this experiment operated exclusively in the OML regime. A preliminary ion number density,  $n_{io}$ , is calculated using Equation (3):

$$n_{io} = -\exp^{0.5} \frac{I_{i,sat}}{eA_p} \sqrt{\frac{M_i}{eT_e}}, \quad (3)$$

where  $I_{i,sat}$  is the ion saturation current and  $A_p$  is the probe surface area. This initial ion number density, combined with electron temperature,  $T_e$ , is used to calculate an initial  $\lambda_D$  using Equation (4):

$$\lambda_D = \sqrt{\frac{\epsilon_0 T_e}{n_{io} e}}, \quad (4)$$

where  $\epsilon_0$  is the permittivity of free space. For OML analysis, two non-dimensional factors  $a = 2\sqrt{\pi}$  and  $b = 1/2$  are used to refine the calculated ion number density,  $n_i$ , as shown in Equation 5:

$$n_i = \frac{1}{aA_p} \sqrt{2\pi m_i} e^{-1.5} T_e^{b-0.5} \left[ \frac{dI_{probe}^{1/b}}{dV_B} \right]^b \quad (5)$$

With the new ion number density, a new  $\lambda_D$  is calculated using Equation (3), and  $n_i$  is recalculated. The process is repeated until convergence of ion number density and  $\lambda_D$  is achieved.

This process was automated using a MatLab script; an example of the data processing is shown in Figure 8. The top plot shows raw current-voltage data, ion saturation region linear fit, raw data with ion current removed, and a polynomial fit to the electron retarding and electron saturation region. The bottom plot shows the log-current to bias voltage plot points with linear fits in the electron saturation region (greater than the plasma potential,  $V_p$ ) and electron retarding region (between the floating potential,  $V_f$ , and  $V_p$ ).

RPA data were collected by sweeping the retarding grid from 0 V to 2100 V and observing the current on the collector plate. The maximum of the first derivative of the RPA collected current with respect to voltage was found with a MatLab post processing script. This point is regarded as the point at which the majority of ion energy exceeds the retarding voltage barrier. In other words, this point is regarded as the most probable ion energy in the ion energy distribution function. Due to the high energy of ions entering the RPA, the electron suppression grid was set to a higher than normal magnitude voltage to limit parasitic current to the collector from secondary electron emission (SEE) and charge exchange collisions; however, the energy profiles still showed clear evidence of these phenomena.

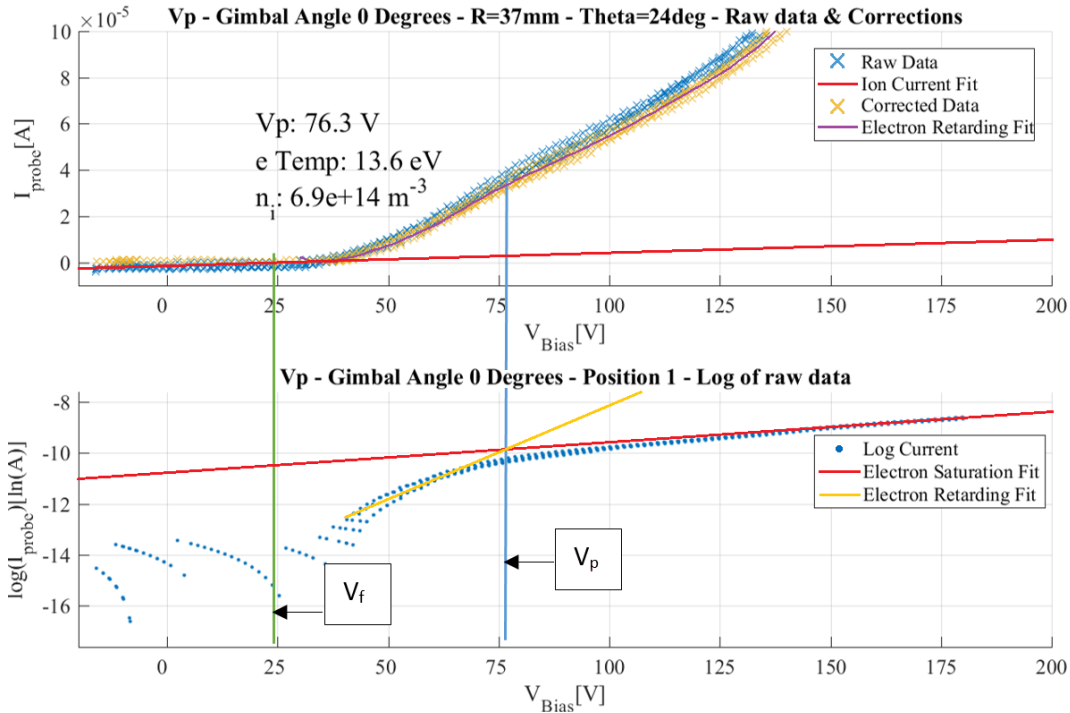


Figure 8. Raw trace data and post processing output of MatLAB script. Markers have been added to the figure to indicate the locations of floating and plasma potentials.

## 4. Results

### 4.1. Telemetry Results

Table 2 presents the averaged telemetry data as a function of gimbal angle.

Approximately 500 telemetry samples were recorded at various magnetorquer positions and averaged. Figure 9 shows the screen and acceleration grid currents and CubeSat chassis floating potential as a function of magnetorquer position within the CubeSat standard. Telemetry data variations are within measurement limitations of the instrumentation.

### 4.2. Faraday Probe Results

Current density maps were created for each gimbal angle of the thruster with respect to the CubeSat chassis. Raw FP data necessitated a geometrical area correction factor due to the difference between the center of rotation of the probe arm and thruster exit plane. Figure 10 shows the normalized current density as a function of downstream location for the zero gimbal angle position and the integration method used to determine beam current. The plasma plume is clearly indicated by the increased current density near the thruster exit axis. Current density as a function of downstream location for gimbal angles of 2°, 5°, and

Table 2. Telemetry Data Results for 0°, 2°, 5°, and 10° Gimbal Angles with Respect to the CubeSat Chassis

| Gimbal Angle, ° | Fwd Pwr, W | Rev Pwr, W | Accel Current, mA | Accel Voltage, V | Screen Current, mA | Screen Voltage, V | Chamber Pressure, Torr | Cube Floating Potential, V |
|-----------------|------------|------------|-------------------|------------------|--------------------|-------------------|------------------------|----------------------------|
| 0               | 7.7        | 1.72       | -0.194            | 218.5            | 1.40               | 1799              | 1.61E-05               | 7.9                        |
| 2               | 7.7        | 1.71       | -0.192            | 218.5            | 1.40               | 1799              | 1.60E-05               | 8.4                        |
| 5               | 7.7        | 1.72       | -0.193            | 218.5            | 1.40               | 1799              | 1.62E-05               | 8.7                        |
| 10              | 7.7        | 1.72       | -0.195            | 218.5            | 1.40               | 1799              | 1.62E-05               | 9.3                        |

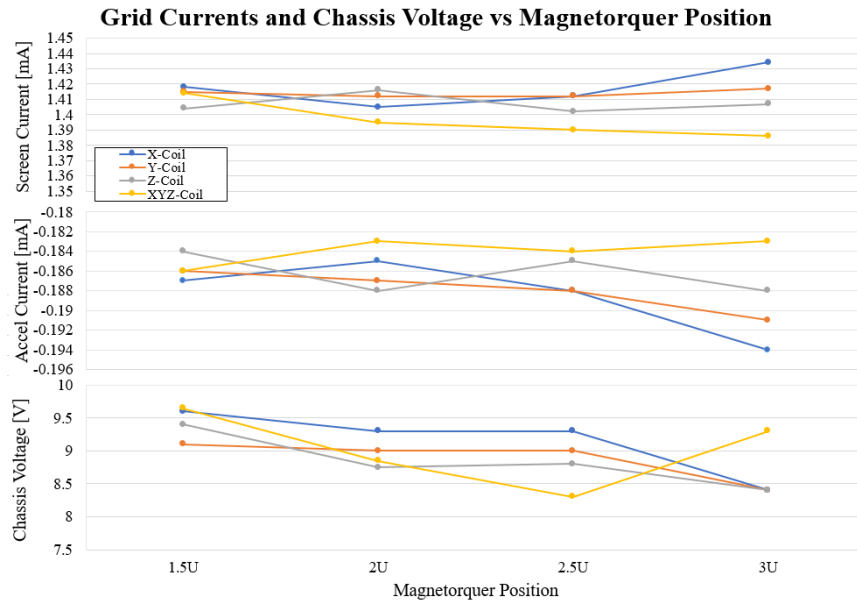


Figure 9. Thruster screen grid current (top), acceleration grid (middle) current, and CubeSat chassis floating potential (bottom) as a function of magnetorquer position and energized coil. Each coil operated at 1.5 A.

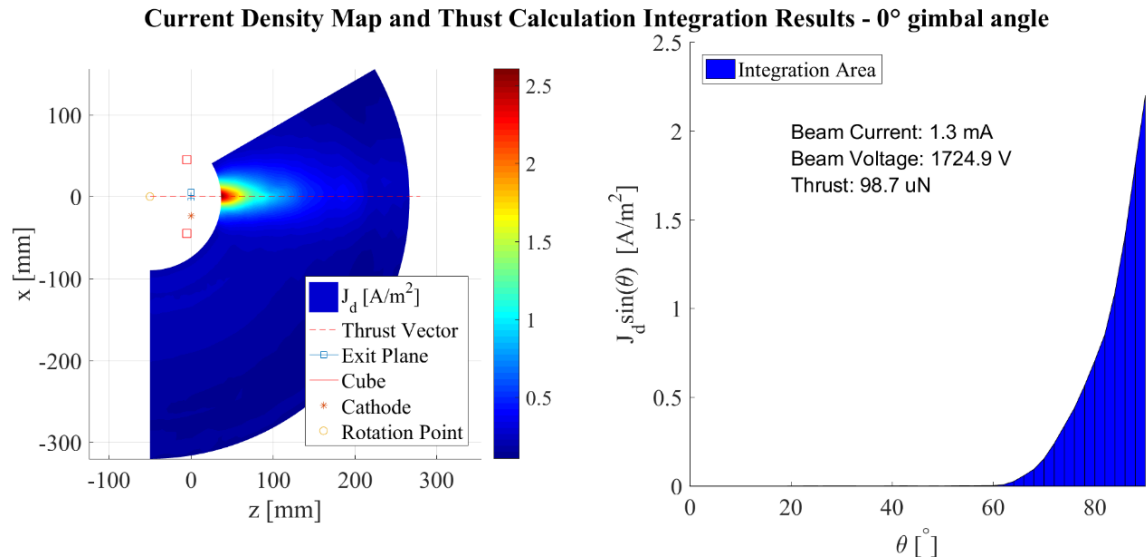


Figure 10. Current density results from an area corrected Faraday probe for 0° gimbaling (left). Corrected Faraday probe current density profile (right). Note that in this plot, the 90° angle corresponds to the angle directly forward the thruster.

10° are shown in the Appendix. The calculated thrust is the magnitude of thrust, not the projection of the thrust vector on to the CubeSat chassis centerline. A summary of the thruster operating characteristics, plasma potential from LP data, beam properties, and thrust magnitude are shown in Table 3. Thrust magni-

tude calculation estimates range from 91.1  $\mu$ N to 122.6  $\mu$ N.

### 4.3. Langmuir Probe Results

Contour maps of LP data are plotted for the floating potential, plasma potential, electron temperature,

Table 3. Summary of Telemetry, Final Beam Properties, and Thrust Calculations for each Gimbaling Angle

| Gimbal Angle, ° | Thruster Telemetry during FP Sampling |      |              |        |             |        |               | LP Data    | Calculated            |                        |            |
|-----------------|---------------------------------------|------|--------------|--------|-------------|--------|---------------|------------|-----------------------|------------------------|------------|
|                 | RF Power, W                           |      | Potential, V |        | Current, mA |        | Pressure Torr | Mean Vp, V | V <sub>Beam</sub> , V | I <sub>Beam</sub> , mA | Thrust, μN |
|                 | Fwd                                   | Rev  | Accel        | Screen | Accel       | Screen |               |            |                       |                        |            |
| 0               | 7.7                                   | 1.61 | -219.9       | 1799   | -0.15       | 1.35   | 1.40E-05      | 73.1       | 1725.5                | 1.3                    | 98.7       |
| 2               | 7.8                                   | 1.60 | -219.9       | 1798   | -0.14       | 1.36   | 1.41E-05      | 77.7       | 1720.4                | 1.2                    | 91.1       |
| 5               | 7.7                                   | 1.61 | -219.9       | 1800   | -0.14       | 1.39   | 1.43E-05      | 75.2       | 1724.6                | 1.5                    | 107.0      |
| 10              | 7.7                                   | 1.62 | -220.0       | 1800   | -0.13       | 1.37   | 1.43E-05      | 82.3       | 1717.5                | 1.7                    | 122.6      |

and ion number density. Figure 11 shows these maps for a gimbal angle of 0°, and maps for 2°, 5°, and 10° are shown in the Appendix. LP I-V traces that collected too little current and showed either no inflection point or knee were discarded. Due to the low mass throughput and low ion number densities developed by the thruster, the typical Debye lengths were on the order of 0.5 to 2.5 mm. Additionally, the typical far field plume floating potentials of this study were 50V higher than previously measured floating potentials (Hine, 2016).

#### 4.4. RPA Results

A retarding potential analyzer (RPA) was used to determine the relative energy levels with the thruster plume at a 0° gimbal angle. RPA data were not collected for other gimbal angles. A second derivative Druyvesteyn method was used to estimate the ion energy probability distribution function of a point inside the plume exiting the thruster (Figure 12a). The point of highest probability was plotted for every spatial RPA data point in Figure 12b.

### 5. Discussion

#### 5.1. Faraday Probe Discussion

To align waveforms for easy comparison, each FP trace was offset on the theta axis by the gimbal angle. This produced Faraday probe sweep data that lay on top of one another, and shows differences between plume shapes at near field (R = 37 mm) and mid-field (R = 97 mm) in Figure 13 for each gimbal angle. The plume divergence is nearly identical near the thruster exit plane for each gimbal angle, and maintains relatively similar divergence shape out to almost 100 mm downstream of the thruster. A small depression in the Faraday probe sweep data is apparent in the current density at the 35° to 40° angle off axis. This corresponds to the location of the cathode, which may have caused a reduction in the current density due to a localized high electron density region. Future higher gimbal angle sweeps could reveal whether the true nature of this depression is due to the asymmetric cathode placement or the CubeSat chassis. Secondary electron emission was not accounted for in the FP data, so the error associated

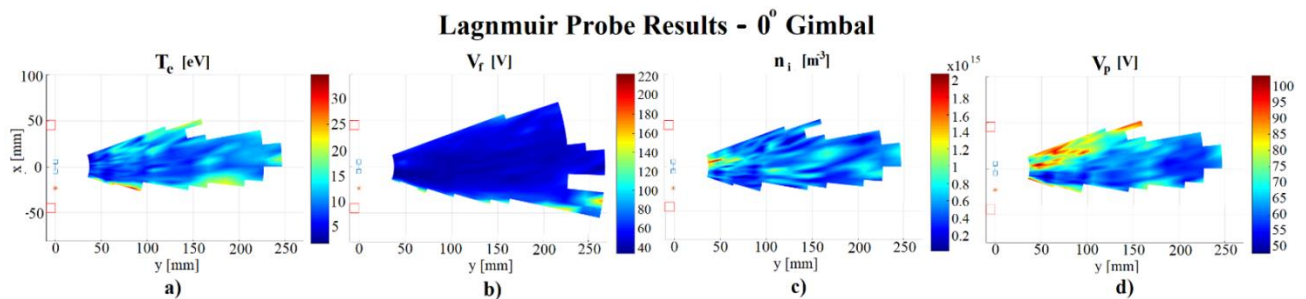


Figure 11. Typical a) electron temperature, b) floating potential, c) ion number density, and d) plasma potential results from Langmuir probe data analysis. Relative location of the CubeSat chassis, thruster exit plane, and cathode location are indicated on the plots.

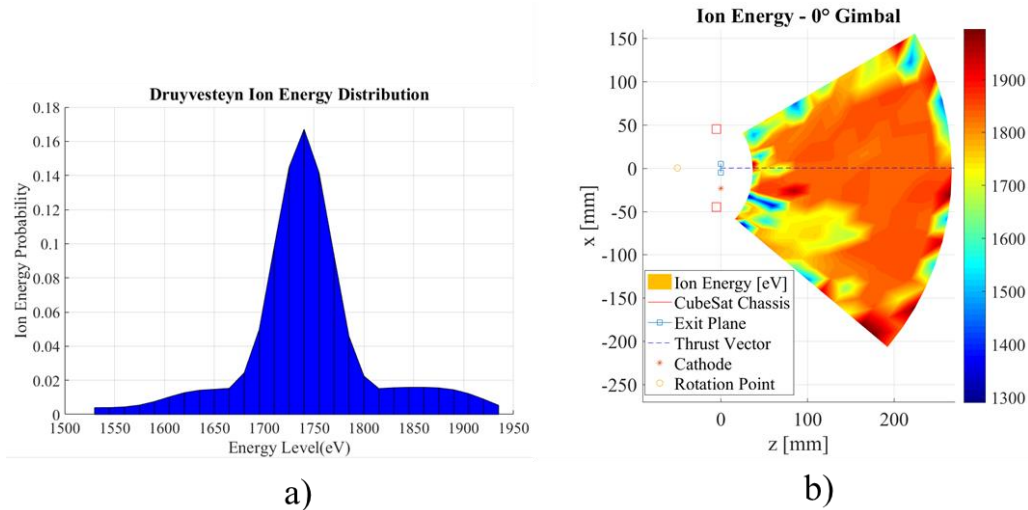


Figure 12. a) Ion energy distribution function 37 mm from thruster exit plane along the thruster centerline. b) Most probable ion energy obtained using an RPA probe for the 0° gimbaling case.

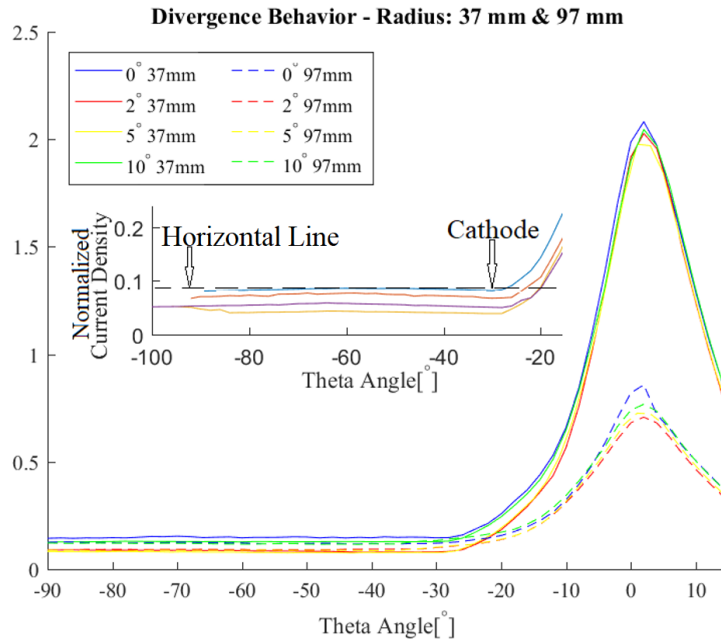


Figure 13. Current density measured by Faraday probe for two downstream locations (37 mm and 97 mm from thruster exit plane) as a function of gimbaling angle. These data are offset such that the 0° angle represents thruster centerline for each gimbaling case.

with FP measurements is estimated at 20% (Brown et al., 2016); therefore, the depression could also be an artifact of the measurement technique and equipment.

## 5.2. LP Discussion

Generally, the LP data are in good agreement with past measurements (Hine, 2016); however, dif-

ferent regions were probed, and a different neutralizer cathode was used, so true comparison of the data sets is difficult. An asymmetry is observable in both the floating and plasma potentials and electron temperature in Figure 11b, c, and d near the thruster exit plane downstream of the thermionic cathode location. This may be caused by the asymmetric cathode placement. Plume variations may also develop due to

the type of cathode used in this experiment. Nominally, xenon gas hollow cathodes are used to neutralize the plume of a xenon ion thruster, rather than barium oxide coated tungsten thermionic heaters. The electron temperature in the plume directly downstream of the thruster ranges from 5 to 15 eV. Debye lengths downstream of the thruster are nominally 1 mm, and the ion number density ranges from  $2 \times 10^{14}$  to  $2 \times 10^{15} \text{ m}^{-3}$ .

### 5.3. RPA Data Discussion

The RPA data map in Figure 12 shows a constant ion energy level in the thruster plume. The mean ion energy level of all RPA data measurements were 1783 eV, and 95% of the measurements fall within  $\pm 200$  eV of the mean ion energy level. A small asymmetry appears as lower ion energy near the cathode. This may be due to excess electrons in the vicinity resulting in ion neutralization. The average measured ion energy is approximately 300 eV less than the anticipated beam voltage, suggesting poor acceleration to the anticipated potential. This may be due to the xenon flow rate being higher than what the thruster was designed for, contributing to excessive neutral charge exchange collisions. Other explanations include the cathode placement and optical degradation of the thruster grids, each of which may contribute to poor ionization fractions and poor performance.

### 5.4. Telemetry Discussion

The first observation regarding telemetry measurements was the increase in CubeSat chassis floating potential as the gimbaling angle increased. This is likely due to increased ion flux to the exposed aluminum surfaces of the chassis. It is also noted that the CubeSat floating potential trended downward as the magnetorquers moved toward the 3U position. This appears independent of other thruster operating parameters, and independent of which coil was energized. The thruster operating conditions were unchanged through all magnetorquer positions and thruster gimbaling angles, suggesting that there is little effect on thruster health and operation during

thruster gimbaling, nor is there a large effect on thruster operation related to the placement of the magnetorquer when combined with an RF gridded ion thruster. Additionally, there appears to be evidence to suggest that there is interference between the thruster and the CubeSat chassis as thrust vector gimbaling angle and magnetorquers' positions are adjusted. CubeSat floating potential ranged from positive 7.9 to 9.3 V, which appears to be influenced heavily by gimbaling angle and possibly by magnetorquer positioning. The increased chassis potential due to increasing gimbal angle may indicate increased spacecraft charging, and this could adversely affect sensitive onboard instrumentation.

## 6. Conclusion/Future Work

There is no noticeable effect on thruster performance due to the configuration of a CubeSat chassis. Telemetry behavior of the thruster is not significantly changed as magnetorquer positions and angle between thruster centerline and chassis centerline change. The maximum change in screen and acceleration grid currents observed during magnetorquer positioning was less than 30  $\mu\text{A}$  and 10  $\mu\text{A}$  respectively, within the measurement limitations of the equipment. Furthermore, there is no noticeable interference on the thruster plume from the CubeSat chassis. However, there is an asymmetry in the plume shape, electron temperature, and plume potentials that is possibly due to the thermionic emitting cathode position. Interestingly, the CubeSat floating potential is increased by 1.4 V as gimbal angle was increased from  $0^\circ$  to  $10^\circ$ , and CubeSat floating potential increased by 1.35 V as the ACS was brought from the 3U to 1.5U position. This suggests that the beam angle and magnetorquer magnetic field could compound adverse effects of the plasma on CubeSat electronics. Interference from magnetorquers could be alleviated by magnetically shielding the CubeSat from the thruster plasma.

Future experiments should include rudimentary circuit elements and PCB's combined with sense lines to detect subsystem susceptibility to reference voltage changes due to spacecraft charging. For future experiments, a hollow cathode or field emission

cathode should replace the AC-powered, BaO-coated heater filament. This will create a more flight-like environment, representing more accurate conditions on-orbit. Permanent magnets could also be included to compare active and passive ACS. It is recommended that the probe sweep angles be expanded to include  $\pm 90^\circ$ , to provide a complete plume map. This could potentially reveal subtle differences in the plume shape due to thrust vectoring. Last, this subject would benefit a great deal from computational modeling. Although this experimental setup was insufficient to investigate the mechanisms behind

CubeSat chassis charging, beam neutralization coupling, and facility effects, perhaps computational modeling could shed light on the root causes of these effects.

**Acknowledgments**

The authors would like to thank the NASA Small Spacecraft Technology Program and Space Technology Mission Directorate (STMD) for their support of this research. This work was supported by a NASA Space Technology Research Fellowship.

**Appendix A  
Supplemental Data: Magnetorquer Position Telemetry**

Table A1. Thruster Telemetry Measurements Recorded at Various Magnetorquer Positions

| MT Position | Axis | RF Power, W |       | Potential, V |        | Current, A |        | Chamber Pressure, Torr | Cube Floating Potential, V |
|-------------|------|-------------|-------|--------------|--------|------------|--------|------------------------|----------------------------|
|             |      | Fwd         | Rev   | Accel        | Screen | Accel      | Screen |                        |                            |
| 1.5U        | X    | 7.66        | 1.72  | -218.5       | 1799   | -0.18      | 1.42   | 1.62E-05               | 9.6                        |
| 1.5U        | Y    | 7.66        | 1.71  | -218.5       | 1799   | -0.19      | 1.42   | 1.62E-05               | 9.1                        |
| 1.5U        | Z    | 7.67        | 1.71  | -218.5       | 1799   | -0.18      | 1.40   | 1.61E-05               | 9.4                        |
| 1.5U        | XYZ  | 7.67        | 1.71  | -218.5       | 1799   | -0.19      | 1.41   | 1.61E-05               | 9.7                        |
| 1.5U*       | XYZ  | 7.67        | 1.71  | -218.5       | 1799   | -0.18      | 1.41   | 1.62E-05               | 9.3                        |
| 2.5U        | X    | 7.68        | 1.72  | -218.5       | 1799   | -0.19      | 1.41   | 1.62E-05               | 9.3                        |
| 2.5U        | Y    | 7.68        | 1.72  | -218.5       | 1799   | -0.19      | 1.41   | 1.62E-05               | 9.0                        |
| 2.5U        | Z    | 7.69        | 1.71  | -218.5       | 1799   | -0.19      | 1.40   | 1.60E-05               | 8.8                        |
| 2.5U        | XYZ  | 7.70        | 1.70  | -218.5       | 1799   | -0.18      | 1.39   | 1.58E-05               | 8.3                        |
| 2U          | X    | 7.68        | 1.71  | -218.5       | 1799   | -0.19      | 1.41   | 1.61E-05               | 9.3                        |
| 2U          | Y    | 7.67        | 1.72  | -218.5       | 1799   | -0.19      | 1.41   | 1.63E-05               | 9                          |
| 2U          | Z    | 7.67        | 1.72  | -218.5       | 1799   | -0.19      | 1.42   | 1.63E-05               | 8.8                        |
| 2U          | XYZ  | 7.69        | 1.702 | -218.5       | 1799   | -0.18      | 1.40   | 1.59E-05               | 8.9                        |
| 3U          | X    | 7.65        | 1.736 | -218.5       | 1799   | -0.19      | 1.43   | 1.66E-05               | 8.4                        |
| 3U          | Y    | 7.68        | 1.724 | -218.5       | 1799   | -0.19      | 1.42   | 1.64E-05               | 8.4                        |
| 3U          | Z    | 7.69        | 1.717 | -218.5       | 1799   | -0.19      | 1.41   | 1.61E-05               | 8.4                        |
| 3U          | XYZ  | 7.71        | 1.698 | -218.5       | 1799   | -0.18      | 1.39   | 1.57E-05               | 9.3                        |

Note: Unless noted otherwise, magnetorquer axis currents set to approximately 1.5 A.

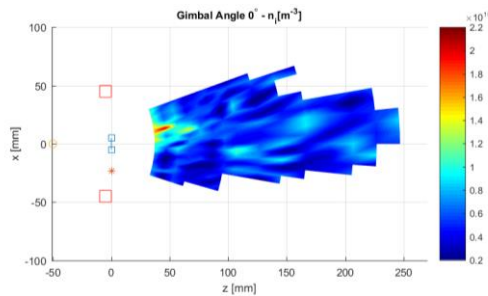


Figure A1. 0° gimbaling ion number density.

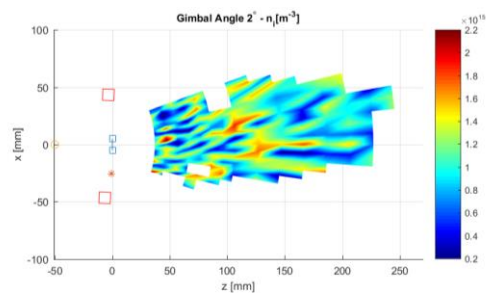


Figure A2. 2° gimbaling ion number density.

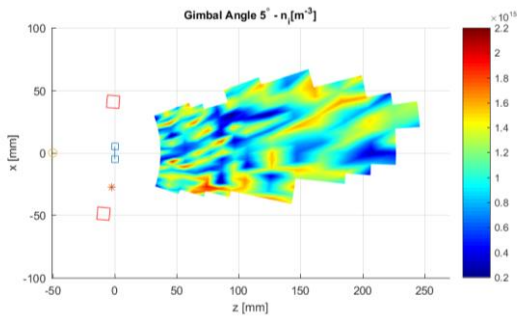


Figure A3. 5° gimbal ion number density.

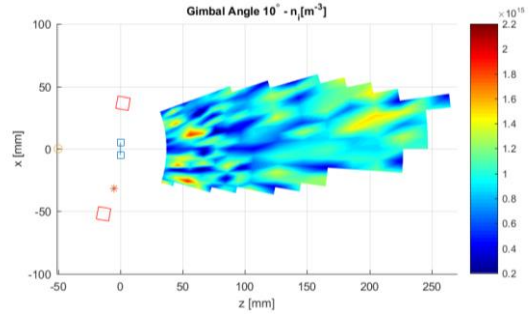


Figure A4. 10° gimbal ion number density.

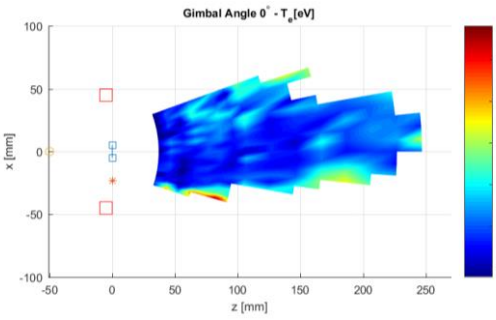


Figure A5. 0° gimbal electron temperature.

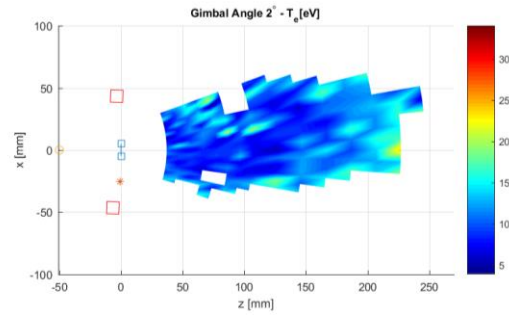


Figure A6. 2° gimbal electron temperature.

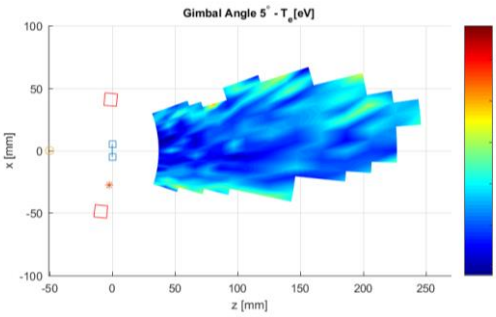


Figure A7. 5° gimbal electron temperature.

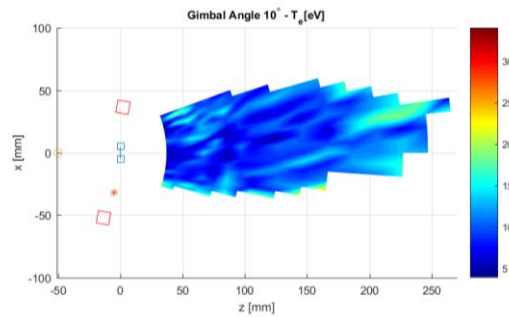


Figure A8. 10° gimbal electron temperature.

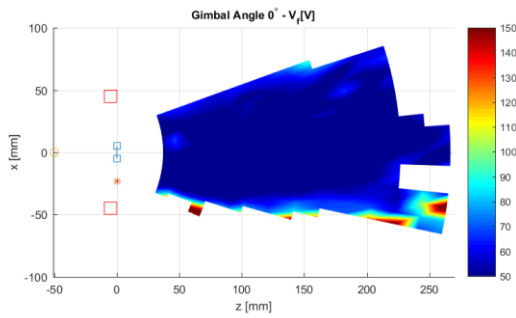


Figure A9. 0° gimbal floating potential.

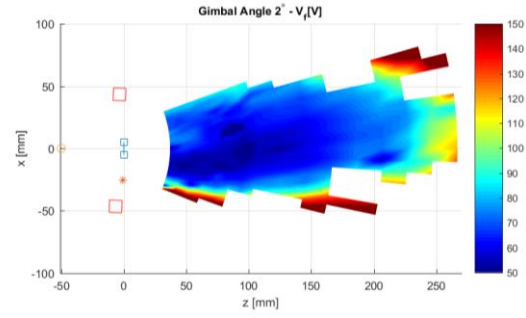


Figure A10. 2° gimbal floating potential.

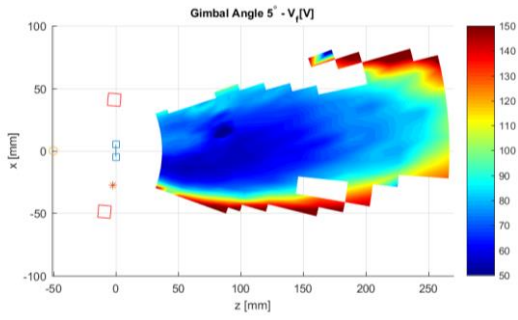


Figure A11. 5° gimballing floating potential.

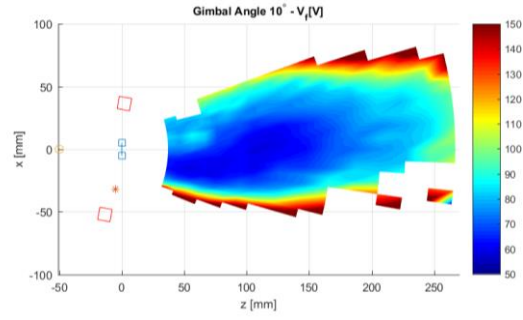


Figure A12. 10° gimballing floating potential.

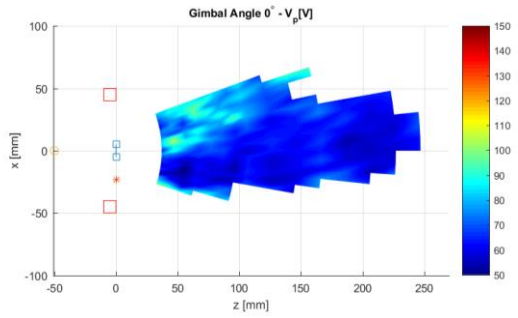


Figure A13. 0° gimballing plasma potential.

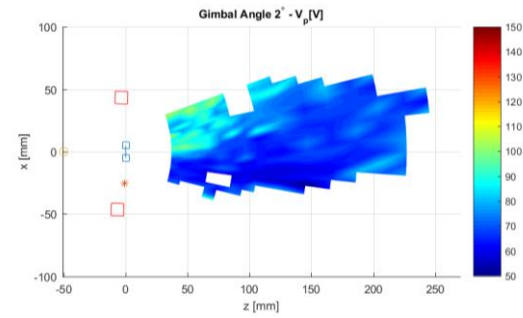


Figure A14. 2° gimballing plasma potential.

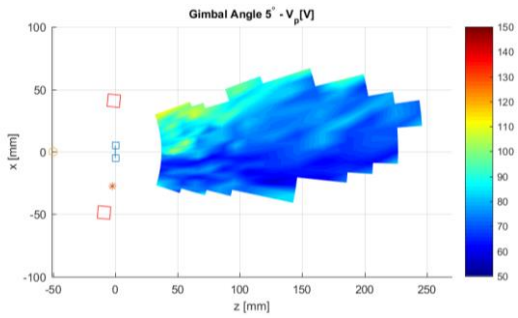


Figure A15. 5° gimballing plasma potential.

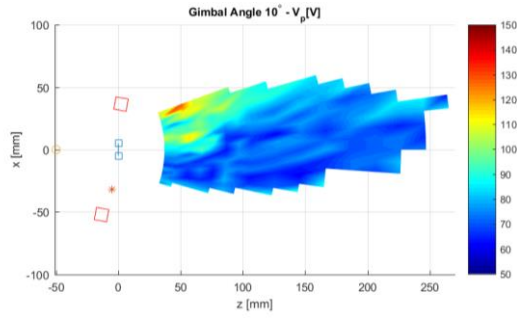


Figure A16. 10° gimballing plasma potential.

## References

- Bani, A. (2016): Design and Analysis of an Axisymmetric Aerospike Supersonic Micro-Nozzle for a Refrigerant-Based Cold-Gas Propulsion System for Small Satellites, Thesis, Dept. of Mechanical and Aerospace Eng., Missouri Univ. of Sci. and Tech., Rolla, MO.
- Brown, L. et al. (2017): Recommended Practice for Use of Faraday Probes in Electric Propulsion. *J. of Propulsion and Power*, Vol. 33 (3), pp. 582–613. doi: 10.2514/1.B35697.
- Candinia, G. P., Piergentilib, F., and Santoni, F. (2012): Miniaturized Attitude Control System for Nanosatellites. *Acta Astronautica*, Vol. 81 (1), pp. 325–34. doi: 10.1016/j.actaastro.2012.07.027.
- Chen, F. (2014): Ion Ejection from a Permanent-Magnet Mini-Helicon Thruster. *Physics of Plasmas*, Vol. 21 (9). doi: 10.1063/1.4896238.
- Gerhardt, D. T. and Palo, S. E. Passive Magnetic Attitude Control for CubeSat Spacecraft. Available at: [http://lasp.colorado.edu/home/csswe/files/2012/06/Gerhardt\\_SSC10\\_PMAC.pdf](http://lasp.colorado.edu/home/csswe/files/2012/06/Gerhardt_SSC10_PMAC.pdf) (accessed July 12, 2017).
- Goebel, D. M. and Katz, I. (2008): *Fundamentals of Electric Propulsion: Ion and Hall Thrusters*, New York: John Wiley and Sons, pp. 1–507. doi: 10.1002/9780470436448.
- Gollor, M. and Boss, M. (2006): Micro-Newton Electric Propulsion Subsystems for Ultra-Stable Platforms, presented at the 30th International Elect. Prop. Conf., Florence, Italy, September 17–20. Paper IEPC-2007-19. doi: 10.2514/6.2006-4825.
- Grönland, T-a. et al. Cubesat Propulsion Module With Closed-Loop Thrust Control. Available at: <https://digitalcommons.usu.edu/> (accessed July 12, 2017).
- Guo, J., Bouwmeester, J., and Gill E. (2016): In-Orbit Results of Delfi-n3Xt: Lessons Learned and Move Forward. *Acta Astronautica*, Vol. 121, pp. 39–50. doi: 10.1016/j.actaastro.2015.12.003.
- HeatWaveLabs Inc. TB-160 Cathode Coatings Types. Available at: [http://www.cathode.com/pdf/TB-160 thru 164.pdf](http://www.cathode.com/pdf/TB-160%20thru%20164.pdf) (accessed January 29, 2017).
- Hine, A. D. (2016): An Exploration of CubeSat Propulsion, Thesis, Dept. of Mechanical and Aerospace Eng., Western Michigan Univ., Kalamazoo, MI.
- Hinkley, D. A Novel Cold Gas Propulsion System for Nanosatellites and Picosatellites. Available at: <http://digitalcommons.usu.edu/cgi/viewcontent.cgi?article=1393&context=smallsat> (accessed July 12, 2017).
- Jayaram, S. (2010): Design of Template to Fabricate Magnetic Torquer Coils for Nano and Picosatellite Missions. *J. of Engineering, Design and Technology*, Vol 8 (2), pp. 158–67. doi: 10.1108/17260531011062537.
- Kronhaus, I. et al. Design of the UWE-4 Picosatellite Orbit Control System Using Vacuum-Arc-Thrusters. Available at: [http://erps.spacegrant.org/uploads/images/images/iepc\\_articledownload\\_1988-2007/2013index/ajvqjr79.pdf](http://erps.spacegrant.org/uploads/images/images/iepc_articledownload_1988-2007/2013index/ajvqjr79.pdf) (accessed July 12, 2017).
- Leigh, W. et al. (2013): Enhanced Performance of Electrothermal Plasma Sources as Fusion Pellet Injection Drivers and Space Based Mini-Thrusters via Extension of a Flat-top Discharge Current. *J. of Fusion Energy*, Vol. 32 (3), pp. 371–77. doi: 10.1007/s10894-012-9578-5.
- Lemmer, K. (2017): Propulsion for CubeSats. *Acta Astronautica*, Vol. 134, pp. 231–43. doi: 10.1016/j.actaastro.2017.01.048.
- Lobbia, R. and Beal, B. (2016): Recommended Practice for Use of Langmuir Probes in Electric Propulsion Testing. *J. of Propulsion and Power*, Vol. 33 (3), pp. 566–81. doi: 10.2514/1.B35697.
- Ovchinnikov, M. et al. (2000): Attitude Control System for the First Swedish Nanosatellite “MUNIN”. *Acta Astronautica*, Vol. 46 (99), pp. 319–26. doi: 10.1016/S0094-5765(99)00226-X.
- Ovchinnikov, M. et al. (2007): Attitude Dynamics of the First Russian Nanosatellite TNS-0. *Acta Astronautica*, Vol. 61 (1–6), pp. 277–85. doi: 10.1016/j.actaastro.2007.01.006.
- Pukniel, A. et al. (2011): The Dynamics and Control of the CubeSail Mission: A Solar Sailing Demonstration. *Advances in Space Research*, Vol. 48 (11), pp. 1902–10. doi: 10.1016/j.asr.2011.07.014.

- Rangsten, P., Bejhed, J., and Johansson, H. Advanced MEMS Components in Closed-Loop Micro Propulsion Applications. Available at: <http://digitalcommons.usu.edu/smallsat/2012/all2012/75/> (accessed July 12, 2017).
- Rankin, D. et al. (2005): The CanX-2 Nanosatellite: Expanding the Science Abilities of Nanosatellites. *Acta Astronautica*, Vol. 57, pp. 167–74. doi: 10.1016/j.actaastro.2005.03.032.
- Rawashdeh, S. A. (2010): Passive Attitude Stabilization for Small Satellites, Thesis, Dept. of Elect. Eng. Univ. of Kentucky, Lexington, KY. Available at: [http://uknowledge.uky.edu/gradschool\\_theses/624](http://uknowledge.uky.edu/gradschool_theses/624).
- Sarda, K. et al. (2006): Canadian Advanced Nanospace Experiment 2: Scientific and Technological Innovation on a Three-Kilogram Satellite. *Acta Astronautica*, Vol. 59, pp. 236–45. doi: 10.1016/j.actaastro.2006.02.054.
- Scholz, A. et al. Flight Results of the COMPASS-1 Mission. Available at: [http://www.crn2.inpe.br/conasat1/projetos\\_cubesat/subsistemas/TEST/COM-COMPASS-1 – TEST – Flight Results.pdf](http://www.crn2.inpe.br/conasat1/projetos_cubesat/subsistemas/TEST/COM-COMPASS-1 – TEST – Flight Results.pdf) (accessed July 12, 2017).
- Springmann, J. C. et al. (2012): The Attitude Determination System of the RAX Satellite. *Acta Astronautica*, Vol. 75, pp. 120–35. doi: 10.1016/j.actaastro.2012.02.001.
- Steyn, W. H. and Lappas, V. (2011): Cubesat Solar Sail 3-Axis Stabilization Using Panel Translation and Magnetic Torquing. *Aerospace Science and Technology*, Vol. 15, pp. 476–85. doi: 10.1016/j.ast.2010.09.009.
- Tsay, M. et al. (2012): Micro Radio-Frequency Ion Propulsion System, presented at the 48th AIAA/ASME/SAE/ASEE Joint Propulsion Conf., Atlanta, GA, July 30–August 1. doi: 10.2514/6.2012-3947.
- Wirz, R. et al. (2008): Hollow Cathode and Low-Thrust Extraction Grid Analysis for a Miniature Ion Thruster. *Int'l. J. of Plasma Science and Engineering*, Vol. 2008.
- Zandbergen, B. T. C. and Cervone, A. (2014): Cubesat Micro-Propulsion Systems for Extending the Capabilities of Academic Projects. 65th Int'l Astronautical Cong., Toronto, Canada, October 12. Paper No. IAC-14.C4.6.1.x23854.